Investigating the electronic structure and bonding in uranyl compounds by combining NEXAFS spectroscopy and quantum chemistry

Clara Fillaux,*[a] Dominique Guillaumont,[a] Jean-Claude Berthet,[b] Roy Copping,†*[c]
David K. Shuh,[c] Tolek Tyliszczak[d] and Christophe Den Auwer[a]

The nature of the reactivity of the "yl" oxygens has been a subject of constant interest for a long time in uranyl chemistry. Thus, the electron-donor ability of the equatorial ligands plays an important role in the nature of the uranyl U=O bond. In this paper, a combination of near-edge X-ray absorption fine structure (NEXAFS) spectroscopy and both ground-state and time-dependent density functional theory (DFT) calculations have been used to examine the effect of equatorial plane ligation on the U=O bonding in two uranyl complexes: $[UO_2(py)_3I_2]$ and $[UO_2(CN)_5][NEt_4]_3$. By coupling experimental data and theory, spectral features observed in the oxygen K-edge NEXAFS spectra have been assigned. Despite the inert character of the U=O bond, we observe that the electron-donating or withdrawing character of the equatorial ligands has a measurable effect on features in the NEXAFS spectra of these species and thereby on the unoccupied molecular orbitals of $\{UO_2\}^{2+}$.

1. Introduction

The remarkable nature of the 5f electrons has stimulated a strong interest in actinide inorganic and coordination chemistry. The electronic structure of actinide molecular compounds has been the subject of numerous theoretical studies. However, the involvement of actinide orbitals in bonding is difficult to determine solely from calculations without any experimental contributions. In particular, there has been much debate over the ability of actinide elements to use their 5f and/or 6d orbitals in chemical bonding.[1–11] One of the particularities of the actinides in their high oxidation states of v and vi is the occurrence, in most cases, of a linear trans dioxo-actinyl cation $\{AnO_2\}^{n+}$, that has short, strong and chemically inert An=O bonds.[12] In the case of uranium(vi), the uranyl core $\{UO_2\}^{2+}$ is characterized by a short U=O bond length (ca. 1.78 Å) in a linear O=U=O geometry which is maintained in the pentavalent state. The $\{UO_2\}^+$ derivatives have slightly longer U=O bonds (ca. 1.82 Å) due to the reduced cationic charge.[13–15] The two major structural characteristics of the uranyl complexes are the linearity of the $\{UO_2\}^{2+}$ moiety, and the coordination of the ligands, in the equatorial plane, perpendicular to the O=U=O axis. However, recent studies under anhydrous conditions have shown that novel coordination geometries of the uranyl ion could be attained with out-of-plane coordination of the ligands[16–21] which may force the $\{UO_2\}^{2+}$ fragment to deviate from linearity.[16,17] Bending to form a cis dioxo-uranyl complex is seriously questioned.[22,23] Chemical activation of the U=O bond of uranyl species is a subject of intense current research. Since it is far beyond the scope of this introduction to describe the panorama of uranyl reactivity, we will focus our discussion on the effect of the equatorial coordination on the U=O bond. For a more extensive discussion, the reader may refer to a specialized review article.[24] It is now clear that the equatorial ligands have a tremendous effect both on the chemical behaviour of the U=O bond and on the U(vi)/U(v) reduction potentials.[12] For a series of neutral complexes it has been reported that strongly donating ligands lead to complexes with larger reduction potentials. The evolution of the infra-red and Raman stretching frequencies of the U=O bond (symmetric and antisymmetric) has been found to be a convenient sign of the electron richness of the complexes.[25] The weakening of the U=O bond, induced by strongly donating ligands, is explained by an increase in the Coulombic repulsion between the uranium center and the two oxygen atoms (thereby increasing their Lewis basicity). Another explanation involves a competition for the 6d uranium orbitals strongly involved in the U=O π*-bond.[26] The purpose of this study is to investigate the effect of equatorial coordination on the U=O bond in the two uranyl complexes: $[UO_2(py)_3I_2]$ and $[UO_2(CN)_5][NEt_4]_3$. Our approach focuses on a combination of experimental (NEXAFS) and theoretical studies of the uranyl bond in these two compounds and how it is influenced by the equatorial ligand, namely the pyridine and the cyanide ones. By combining these two approaches, it enables one to quantitatively describe the molecular orbitals involved in uranyl bonding. Accordingly, the two equatorial ligands described here have been chosen due to their different donor–acceptor character. CN is known to act as a strongly electron-donating ligand whereas pyridine induces weaker interactions. Finally X-ray absorption

[a] CEA, DEN, DRCP, 30207 Bagnols sur Cèze, France.
  E-mail: clara.fillaux@cea.fr; Fax: +33 (0)4 66 79 6325;
  Tel: +33 (0)4 66 79 65 87
[b] CEA, CNRS, IRAMIS, UMR 3299 SIS2M, F-91191 Gif Sur
  Yvette, France
[c] Chemical Sciences Division, Lawrence Berkeley National
  Laboratory, Berkeley, CA 94720, USA
[d] Advanced Light Source Division, Lawrence Berkeley National
  Laboratory, Berkeley, CA 94720, USA
† Present address: CEA, DEN, DRCP, 30207 Bagnols sur Cèze,
France

spectroscopy (XAS) as well as quantum chemical calculations are two of the few techniques that enable the study of bond character by yielding information about the electronic structure of the complexes.

There has been considerable interest in the use of synchrotron-based near-edge X-ray absorption fine structure (NEXAFS) spectroscopy for understanding aspects of the electronic structure in the study of materials. These include, for example, oxidation states, charge transfer, and the nature of the low-energy excited states.[27–30] However, interpretation of NEXAFS spectra is a difficult task. The features seen around the edge must be compared to reference compounds (fingerprint analysis) or to theoretical calculations, in order to understand the relationship between the spectral features and the electronic or geometric intra-molecular structure. Multiple-scattering NEXAFS is more challenging than EXAFS calculations, since the photoelectron has sufficiently low kinetic energy making it sensitive to the details of the potential shape and thus to the details of the electronic structure. Therefore, particular attention is often given to the lowest-energy part of the spectrum, *i.e.*, the first few eVs around the edge. Spectral features sensitive to electronic and geometrical parameters are present in this energy range.

To obtain quantitative information from the experimental results, we performed electronic structure calculations and NEXAFS simulations of the two compounds at the oxygen K-edge of the transdioxo unit. FDMNES[31] and ADF[32] codes were used, based on density functional theory (DFT). FDMNES is dedicated to XAS simulation whereas ADF performs quantum chemistry calculations. Furthermore, to complete those simulations, core-electron excitation energies have also been computed using molecular time-dependent density functional theory (TD-DFT) as implemented in the ADF code. The close interplay between experimental measurements and theoretical analysis has been and continues to be one of the most fruitful approaches to our present understanding of the electronic structure of condensed matter.[33,34]

Furthermore, coupling ground-state electronic structure calculations and NEXAFS simulations will provide a quantitative interpretation of the observed NEXAFS spectra. In uranyl atoms, there is covalent bonding between oxygen and the uranium cation, this means that the O 2p orbitals have empty antibonding part due to hybridization with empty U orbitals, that is likely to be investigated in an oxygen K-edge NEXAFS experiment, as it involves a 1s–2p electronic transition, according to the dipole selection rules. Electron-donating/withdrawing properties of the equatorial ligands cause significant changes to transition energies and intensities, which can be explained with the aid of DFT calculations.

2. Experimental details

2.1 Synthesis

$[UO_2(py)_3I_2]$ (**1**) and $[UO_2(CN)_5][NEt_4]_3$ (**2**) are two uranyl compounds with equatorial ligands each possessing different donor–acceptor character.[35,36] In the two compounds, the uranium atom is found in the classical pentagonal bipyramidal configuration. In the structure of **1** and **2**, the linear $\{UO_2\}^{2+}$

fragment is perpendicular to the equatorial plane defined respectively by three nitrogen atoms of the pyridine ligands, two non-adjacent iodide groups, and five carbon atoms of the cyanido ligands. **1** and **2** exhibit quite similar U=O bond lengths: 1.76 Å and 1.77 Å respectively. The U–N bond lengths in **1** average 2.54 Å, while the mean U–C distance is 2.57 in **2**. Finally, the U–I distances are around 3.12 Å in **1**.

2.2 NEXAFS data collection

At the Advanced Light Source, the Molecular Environmental Science (ALS-MES, Lawrence Berkeley National Laboratory, USA) beamline 11.0.2 scanning transmission X-ray micro-scope (STXM) was used to perform NEXAFS on samples **1** and **2**. Soft X-ray STXM is well suited for the investigation of actinides or other radioactive materials since the amount of material required is very low.[37] It offers the opportunity to investigate radioactive samples in an efficient and safe way. In our experiments, the samples were finely ground and the polycrystalline powder was dispersed onto a 50 nm silicon nitride window. Then, a second 50 nm window was sealed to the first and the sample package was attached to the sample holder. The available energy range was approximately 90–2150 eV and the energy resolution of the measurements was approximately 0.11 eV at the oxygen K-edge.

2.3 Ground-state DFT and time-dependent DFT calculations

DFT and TD-DFT calculations were performed with an ADF program package.[32] Relativistic effects were taken into account through the zeroth-order regular approximation (ZORA).[38] All electrons were described using a basis set of uncontracted triple-ζ Slater-type orbitals with two sets of polarization functions (TZ2P). Unless otherwise mentioned, the gradient-corrected BP86 functional was employed.[39,40] The numerical integration parameter setting the numerical integration accuracy in ADF was set at 6.0.

Structural parameters used in the DFT and TD-DFT calculations reported on $[UO_2(CN)_5]^{3-}$ and $[UO_2(py)_3I_2]$ were derived from their crystal structure. The geometries of both complexes were optimized through DFT calculations, the optimized bond distances with uranium were slightly longer than X-ray distances (by a few hundredths of an Å). The crystal structure rather than the DFT-optimized structure was preferred in order to be coherent with the FDMNES simulations. However, it was checked that the results (electronic structure and excitation energies) of optimized and crystal structures were similar.

Electronic atomic charges and atomic orbital populations were deduced from Mulliken analysis and from a natural population analysis (NPA). For the NPA analysis, the NBO 5.0 program was used.[41]

TD-DFT[42,43] calculations were performed allowing only excitations from the localized oxygen 1s orbitals on the absorber atom in order to avoid computation of the whole spectrum.

In a series of test calculations, transition energies were computed using various approaches on isolated uranyl species for the optimized $\{UO_2\}^{2+}$ structure which corresponds to a U=O bond length of 1.72 Å with the BP86 functional and TZ2P basis set. A calculation of isolated uranyl was also done with a U=O bond length of 1.76 Å because in the crystal

structure of $[UO_2(CN)_5]^{3-}$ and $[UO_2(py)_3I_2]$, the U=O bond lengths are 1.77 and 1.76 Å respectively. For ΔSCF and Slater transition-state results, calculations were performed with the proper broken symmetry to achieve localized core-hole state solutions. The symmetry of the $\{UO_2\}^{2+}$ was lowered from $D_{\infty h}$ to C_{2v}. It should be emphasized that with a conventional basis set such as the one used here, only transitions towards discrete electronic levels are properly described, unbound states cannot be properly described.

Spin-orbit effects were not included in the present calculations partly to avoid the use of double-group symmetry to describe the molecular orbitals involved in the transitions. One TD-DFT calculation was done on $\{UO_2\}^{2+}$ with spin-orbit coupling (SOC) as implemented in ADF. Transition energies from oxygen 1s orbitals were weakly affected by SOC.

2.4 XANES calculations with FDMNES

In ref. 31, NEXAFS spectra were simulated with the FDMNES code. The calculations were based on DFT with a local-density approximation. Two methods of calculation are available in the FDMNES code: the multiple scattering theory with the muffin-tin approximation on the potential (MS-MT) and the finite difference method (FDM) using a completely free potential shape. MS-MT is the most commonly used method, however, the muffin-tin approximation may be very limiting at low photoelectron kinetic energies and for compounds with low symmetry.[27] When this method of calculation is not satisfactory, one can use the finite difference method to get rid of the muffin-tin approximation. Since it allows a completely free potential shape, the FDM is more realistic than the MS-MT approach. However, as the FDM is computationally intensive, it has to be used herein only in case of MS-MT calculation failure.

In this study, preliminary XANES simulations were carried out in the framework of the MS-MT approach, without giving satisfactory results. Then the FDM was used to go beyond the muffin-tin approximation, as shown in the remainder of this paper. Since a self-consistent field is not yet implemented in the FDMNES code for the finite difference method, the calculations have been performed without self-consistency and without any fitting procedure. The user input data was the atomic positions and the number of electrons in valence orbitals of each atom. The structural parameters were known from X-ray diffraction experiments and they were kept unchanged for all the calculations.[35,36] On the other hand, atomic charges and orbital populations were calculated with the ADF package and then used as input parameters in the FDMNES code. Hence, the electronic configuration has been tuned to get the best simulated spectra. Moreover, to reproduce the core-hole lifetime broadening, the calculated spectra are convoluted by a Lorentzian function which width increases with the energy (0.2 eV at the Fermi level).

3. Results and discussion

3.1 Experimental spectra

During the photoelectric process, the spectrum on an absorption edge is intrinsically broadened because of the
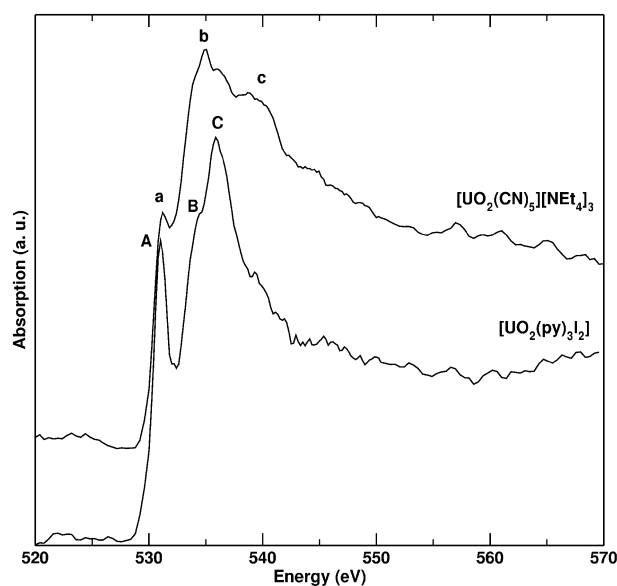
Fig. 1 Oxygen K-edge transmission NEXAFS spectra collected for the two uranyl compounds $[UO_2(py)_3I_2]$ and $[UO_2(CN)_5][NEt_4]_3$. The spectra are vertically offset for better comparison.

creation of a core-hole with a given lifetime. This lifetime depends on the absorbing element and on the absorption edge; the shorter the core-hole lifetime, the broader the experimental spectrum.[44] As an example, the intrinsic broadening for the uranium L_3-edge is ~ 7 eV, whereas it is 0.2 eV for the oxygen K-edge. The information contained in the uranium L_3-edge is hidden by the large broadening, whereas it can be extracted from less broadened spectra such as oxygen K-edge. This specificity makes the K-edge of the light elements particularly relevant to study the electronic structure of the compounds studied herein.

The oxygen K-edge NEXAFS spectra of $[UO_2(py)_3I_2]$ (1) and $[UO_2(CN)_5][NEt_4]_3$ (2) particles are shown in Fig. 1. Although oxygen absorber atoms are 'yl' oxygen atoms in both 1 and 2 (i.e., they belong to an uranyl unit O=U=O), the oxygen K-edge NEXAFS spectra are significantly different from each other. We can distinguish three main features in both spectra. However, the features differ in energy, relative intensity and broadening. There is a clear pre-edge feature located at 531.0 eV (A), a shoulder on the main absorption threshold at 534.4 eV (B), and the main broad absorption band is centred around 535.9 eV (C) for $[UO_2(py)_3I_2]$. The $[UO_2(CN)_5][NEt_4]_3$ spectrum exhibits a pre-peak at the energy of 531.2 eV (a), with a lower intensity relative to the main absorption feature in $[UO_2(py)_3I_2]$, and two broad bands at 535.0 (b) and 539.9 eV (c). The main differences are in the position and broadening of peaks (c) and (C) and in the relative intensities of the features. In this study, the oxygen K-edge spectra give a representation of the vacant molecular orbital containing oxygen 2p character of the uranyl unit for each compound. Even though the U=O bond is strong and its length is almost unchanged, its electronic structure seems to be affected by the identity of the equatorial ligand.

This journal is © the Owner Societies 2010

Phys. Chem. Chem. Phys., 2010, **12**, 14253–14262 | 14255

3.2 Electronic ground-state calculations
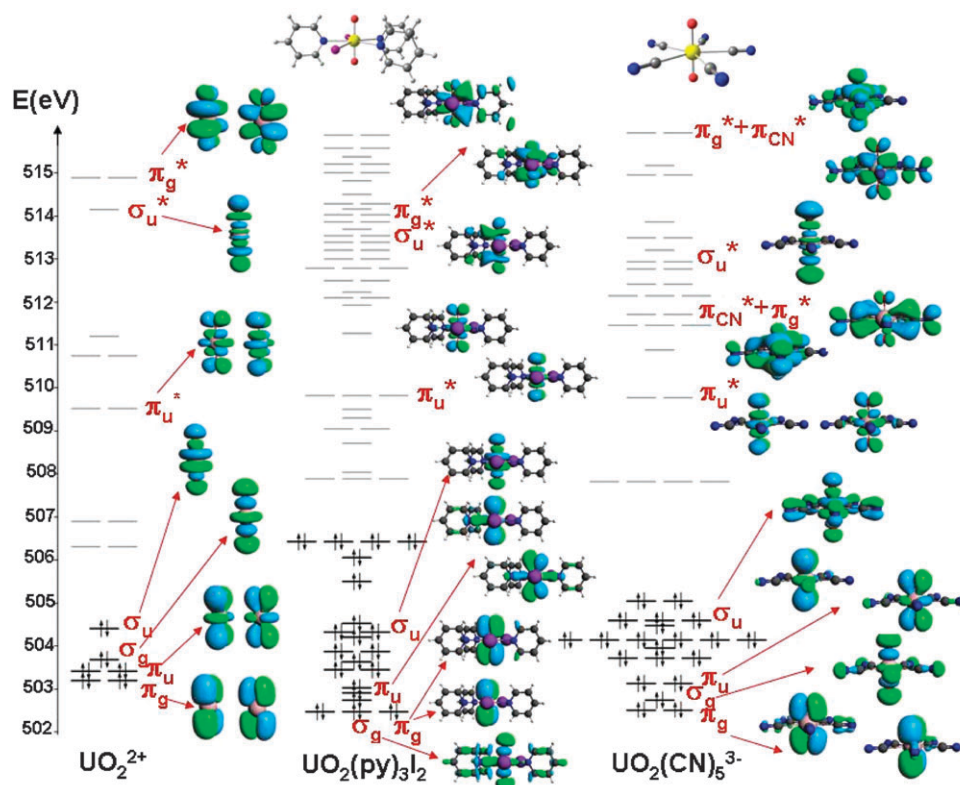
Ground-state DFT calculations were performed on $[UO_2(CN)_5]^{3-}$ and $[UO_2(py)_3I_2]$ to obtain electronic charges and orbital populations which are used in the FDMNES simulations and to compare the electronic structure of uranyl in the two complexes. For $[UO_2(CN)_5]^{3-}$, no NEt$_4$ counterions were included since they are not directly coordinated to uranium.

Before describing the electronic structure of uranyl in the complexes, it is helpful to recall that uranyl has a $\pi_g^4\pi_u^4\sigma_g^2\sigma_u^2$ valence electronic configuration in its ground state.[1] The σ_u and π_u have mostly uranium 5f and oxygen 2p contributions whereas σ_g and π_g have mostly uranium 6d and oxygen 2p contributions. The lowest unoccupied molecular orbitals are π_u^*, σ_g^*, σ_u^* and π_g^*.

The bonding of a cyanide ligand to uranyl has been previously described by Sonnenberg *et al.* from DFT calculations.[45] It was shown that cyanides preferably bind uranium through their carbon atoms and that they interact through σ- and π-donation. On the other hand, because of its relative orientation toward uranyl, pyridine is only capable of interaction with uranyl through its σ molecular orbitals (see Fig. 2). Occupied molecular orbitals are shown on the valence MO diagram in Fig. 2 for **1** and **2**. It shows the interaction of a uranyl fragment with pyridine and cyanide ligands. It also confirms the ability of cyanide ligands to interact with uranyl through σ and π donation; π_{CN} orbitals of cyanide interact

with π_g and σ_u whereas σ orbitals interact mostly with σ_g and slightly with π_u. The pyridine ligand is only capable of σ donation mostly towards π_u and σ_g. Finally, the energy order of the uranyl occupied molecular orbitals in the two complexes is π_g (O 2p–U 6dπ) < σ_g (O 2p–U 6dσ) < π_u (O 2p–U 5fπ) < σ_u^* (O 2p–U 5fσ). In the pyridine complex, π_g and σ_g are nearly degenerate.

For unoccupied MOs, the diagram in Fig. 2 also shows σ and π interactions between cyanide and uranyl and only σ interactions between pyridine and uranyl. In both compounds, the σ_g^* orbital interacts strongly with σ-type orbitals of the ligands and is split among several orbitals. Therefore, it is difficult to ascribe any particular orbital to σ_g^*. In both systems, the energy order of the uranyl unoccupied MO follows the order determined for isolated uranyl,[1] with π_u^* (O 2p–U 5fπ) < σ_u^* (O 2p–U 5fσ) < π_g^* (O 2p–U 6dπ). However, the energy differences between the unoccupied molecular orbitals differs between the two complexes. Compared to isolated $\{UO_2\}^{2+}$, the uranyl σ_u^* is slightly stabilized in the presence of pyridine and even slightly more with cyanide by a few tenths of an eV. The most significant difference comes from the π_g^* orbitals in the cyanide complex, its strong interaction with cyanide π_{CN}^* orbitals split the π_g^* into two molecular orbitals; one at lower energy which is predominantly π_{CN}^* and one at higher energy which is predominantly π_g^*. In the pyridine complex, the π_g^* orbital is only slightly stabilized because of σ-type interactions.

Fig. 2 Molecular orbital diagram of $[UO_2(CN)_5]^{3-}$ (left) and $[UO_2(py)_3I_2]$ (right) showing the interaction of a uranyl fragment with pyridine and cyanide ligands, obtained from ground-state DFT calculations (BP86). Plots of molecular orbitals localized on the uranyl fragment are represented (symmetry labels are for $D_{\infty h}$ symmetry). Energies are relative to the oxygen 1s orbitals.

3.3 Electronic excited-state calculations

Within DFT, there are several approaches to compute core-electron excitations. In the ΔSCF approach, energies are calculated from the difference between the ground-state total energy and that of the excited states in the presence of the core-hole. In the Slater transition-state method, initial and final states are described within the same set of orbitals and obtained by removing half an electron from the core orbital and by adding half an electron to the empty orbital.[46,47] Within the TD-DFT formalism[48] all excitation energies are obtained from one calculation and core excited states are determined by restricting the single excitation space to include only excitations from a subset of core orbitals.[42] In TD-DFT calculations, relaxation effects for the occupied molecular orbitals in the excited state are not taken into account. However, recent studies have shown that TD-DFT can be a simple and useful approach to estimate core-electron excitation energies and to help in the interpretation of NEXAFS spectra.[42,49,50] It has been applied for the first time to the Cl K-edge of thorium in metallocene dichlorides. Transitions from Cl 1s orbitals into empty metal-based orbitals containing 3p character were computed and from the comparison between calculated and experimental spectra, the contribution of metal orbitals in M-Cl bonding was evaluated.[51]

In the present study, we have used TD-DFT to study core excitation from oxygen 1s orbitals. However, before applying TD-DFT to uranyl complexes **1** and **2**, preliminary calculations were performed on isolated $\{UO_2\}^{2+}$ in order to investigate the influence of the chosen density functional and to compare the results with those obtained using a ΔSCF approach or the Slater transition-state method.

Denning et al. have shown that the oxygen Kα spectrum in $[Cs][UO_2Cl_4]$ has four features near 530 eV which have been assigned to transitions toward the antibonding π_u^*, σ_g^*, σ_u^* and π_g^* uranyl molecular orbitals. It has been further shown that there are three intense transitions towards π_u^*, σ_u^* and π_g^* and the transition toward σ_g^* is weak. Denning et al. have calculated oxygen Kα excitation energies in $[UO_2Cl_4]^{2-}$ using a ΔSCF approach and have obtained very good agreement with transition energies measured in $[Cs][UO_2Cl_4]$.[1]

Calculated transition energies are reported in Table 1. Oscillator strengths obtained from the TD-DFT calculations are reproduced in Table 2. Core-hole relaxation effects are not present in TD-DFT calculations whereas they are taken into account when using ΔSCF and transition-state methods. As a consequence, TD-DFT energies are $\sim$20 eV smaller than

Table 2 Calculated oscillator strengths obtained from TD-DFT

Method	1s → π_u^*	1s → σ_g^*	1s → σ_u^*	1s → π_g^*
TD-DFT (BP86)	0.054	0.003	0.048	0.067
TD-DFT (BP86) QZ4P	0.054	0.003	0.048	0.066
TD-DFT (SAOP)	0.044	0.003	0.046	0.066

ΔSCF and transition-state values. However, rather than absolute values, energy shifts between the peaks are more relevant to interpret XANES features and the three computation schemes provide close values for those. The difference in energy shifts between the two methods tends to increase with the transition energy but is always less than 2 eV. The good agreement between TD-DFT and ΔSCF or transition-state calculations is coherent with the absence of strong configuration mixing in TD-DFT results.
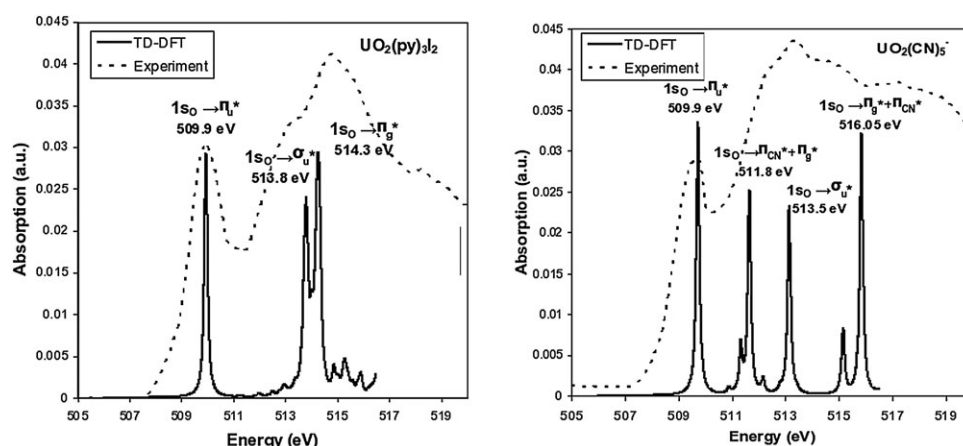
Within TD-DFT calculations, the impact of the functional and the size of the basis set was tested using SAOP[52] instead of BP86, and QZ4P instead of TZ2P. QZ4P is the largest basis set available for actinides in ADF. SAOP has a correct asymptotic behaviour and has been developed in order to better represent high-energy unoccupied molecular orbitals such as Rydberg orbitals. None of these changes have a significant effect on transition energies and oscillator strengths.

TD-DFT simulated spectra corresponding to O1s core excitations are shown in Fig. 3. For the two compounds, the TD-DFT transition energies follow the order of the unoccupied molecular orbitals with significant oxygen 2p contribution. The first peak corresponding to the transition towards the π_u^* appears at the same energy for the two compounds (509.9 eV). A very similar energy was found for uranyl (510 eV) when using the same level of calculation. This is consistent with the very small interaction of this orbital with those of the pyridine or cyanide ligands. The transition energy towards the σ_u^* is calculated at a slightly lower energy for the cyanide uranyl compound than for $[UO_2(py)_3I_2]$. This reflects the slightly stronger interaction of σ_u^* with cyanide π-type orbitals than with pyridine σ-type orbitals. However, the most significant difference arises from the transitions toward the π_g^* orbitals which give rise to very different features in the spectra. The strong interaction with cyanide π^* orbitals splits the uranyl π_g^* into two molecular orbitals: $\pi_g^* + \pi_{CN}^*$ and $\pi_{CN}^* + \pi_g^{\overline{*}}$ (see Fig. 2). It results in one low-energy transition calculated at 511.8 eV toward the cyanide π_{CN}^* orbital with significant π_g^* contribution ($\pi_{CN}^* + \pi_g^*$), while the transition toward the $\pi_g^{\overline{*}} + \pi_{CN}^*$ orbital is shifted to a higher energy. The pyridine

Table 1 Comparison of oxygen 1s core-excited energies (eV) obtained from ΔSCF, TD-DFT and Slater's transition-state methods for $\{UO_2\}^{2+}$. Energy shifts relative to the lowest transition energy are given in parentheses

Method	1s → π_u^*	1s → σ_g^*	1s → σ_u^*	1s → π_g^*
ΔSCF (BP86)	531.8	533.8 (+2)	536.7 (+5.5)	537.3 (+6.1)
Transition state	533.8	535.6 (+1.8)	538.6 (+4.8)	539.0 (+5.2)
TD-DFT (BP86)	510.0	511.4 (+1.4)	515.6 (+5.6)	516.9 (+6.9)
TD-DFT (BP86) QZ4P	510.0	511.4 (+1.4)	515.6 (+5.6)	516.9 (+6.9)
TD-DFT (BP86)[a]	509.5	511.1 (+1.6)	513.9 (+4.4)	514.8 (+5.3)
TD-DFT (SAOP)	509.8	510.6 (+0.8)	514.7 (+4.9)	516.3 (+6.5)

[a] U=O distance is equal to 1.79 Å where it is equal to 1.72 Å otherwise.

This journal is © the Owner Societies 2010

Phys. Chem. Chem. Phys., 2010, **12**, 14253–14262 | 14257

Fig. 3 TD-DFT simulation of oxygen K-edge spectra for $[UO_2(CN)_5]^{3-}$ (right) and $[UO_2(py)_3I_2]$ (left). TD-DFT spectra are simulated by broadening the calculated transitions as a sum of Lorentzian functions with peak widths of *ca.* 0.1 eV. The experimental spectra are shifted in energy to match the calculated spectra.

also interacts with π_g^* but the interaction is not strong enough to give rise to a new peak in the spectrum. The comparison between TD-DFT simulated and experimental spectra is reproduced in Fig. 3. The experimental spectra have been shifted to lower energy and TD-DFT spectra are simulated by broadening the calculated transitions as a sum of Lorentzian functions with small peak widths of *ca.* 0.1 eV. No energy-dependent Lorentzian convolution was used.

As described for the isolated uranyl unit, neglecting the core-hole relaxation effects at this level of calculation leads to an underestimation of absolute transition energies. Fig. 3 shows that the energy shifts between the peaks are also underestimated in the TD-DFT calculations. This energy shift could be due to the absence of core-hole relaxation effects, however the calculations on isolated uranyl have shown that these effects have a small influence on the energy shifts of oxygen K-edge. Other effects such as the absence of inelastic losses in our model can explain this underestimation. In addition, it should be remembered that the calculations are performed using a basis set of Slater-type orbitals whose size is limited and the orbitals become less and less appropriate as the energy of the final molecular orbital or final state increases.

3.4 Simulation of oxygen K-edge spectra with FDMNES

As already mentioned in 3.1., the oxygen K-edge is very sensitive to the electronic structure of the studied compounds, because of its long core-hole lifetime. Thus the shape of the experimental spectra is mainly influenced by the electronic configuration of the two compounds described in this paper.[33,34] To emphasize this phenomenon, several calculations have been performed with different sets of charges: neutral

Table 3 Mulliken/NPA populations for $[UO_2(py)_3I_2]$ valence s, p, d and f shells

| Atom	Charge	s	p	d	f
U	+1.9/+1.3	0.02/0.29	5.71/6.0	1.60/1.77	2.77/2.73
O	−0.6/−0.7	1.90/1.81	4.66/4.78	0.05/0.01	—
N	−0.5/−0.5	1.55/1.32	3.89/4.13	0.07/0	—
I	−0.5/−0.4	1.98/1.91	5.47/4.44	0.04/0	—

Table 4 Mulliken populations for $[UO_2(CN)_5][NEt_4]_3$ valence s, p, d and f shells

Atom	Charge	s	p	d	f
U	+1.2	0.21	0.10	1.85	2.60
O	−0.7	1.91	4.70	0.05	—
C	−0.1	1.50	2.56	0.05	—
N	−0.4	1.65	3.68	0.05	—

atoms, and atomic charges calculated with ADF (see 3.2. and Table 3–4).

The absorption spectra of $[UO_2(py)_3I_2]$ were simulated by the FDMNES code using a FDM. As this procedure is very time consuming, we used a 4.5 Å radius cluster, including 17 atoms. Since the two oxygen atoms in the molecule are equivalent, the choice of the absorbing atom is arbitrary. The convoluted spectra are superimposed in Fig. 4a, for different sets of charges, after being shifted in energy to match the experiment (−0.5 eV for the simulation with Mulliken charges, −2.5 eV with NPA charges and −9 eV with neutral atoms). Very good agreement with the experimental spectrum is obtained with the Mulliken charges. The energy separations of spectral features are especially well reproduced, although their amplitude distribution presents some discrepancies with the experimental ones. The spectrum calculated with the Mulliken charges is the only one exhibiting the three main structures A, B and C. On the other hand, calculations with neutral atoms or NPA charges show only two features having the wrong relative energy position. However, note that the simulated spectrum with NPA charges shows a double peak at around 534 eV before the core-hole lifetime convolution was performed. The two peaks are separated by 0.7 eV and they lead to a single peak after the convolution. This effect is not observed in the case of the calculation with neutral atoms. Thus, despite the closeness of the electronic configurations given by NPA and Mulliken analysis (Table 3), the corresponding oxygen K-edge features are radically different. As it concerns the Fermi level, one can see the same tendencies in the spectrum shape: its simulation is very poor with neutral atoms whereas it improves with NPA and Mulliken charges. The spectrum simulated with Mulliken charges is only shifted
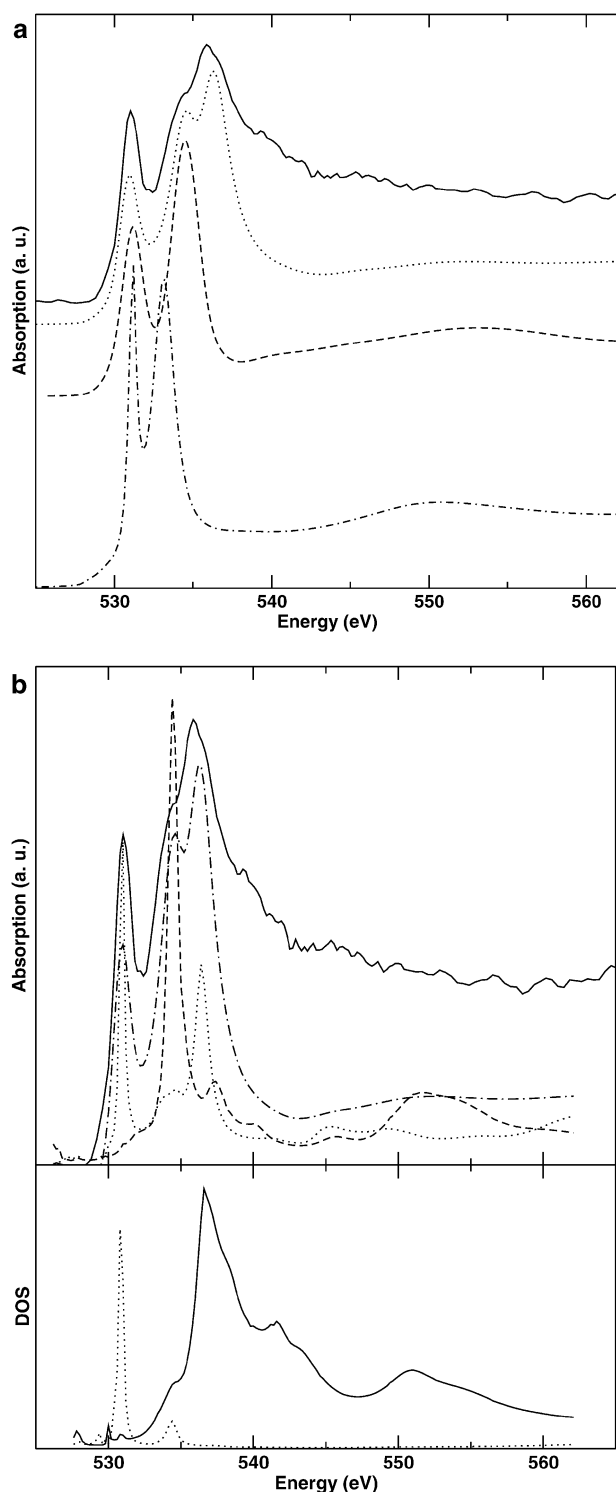
Fig. 4 (a) Experimental and calculated oxygen K-edge spectra of [UO$_2$(py)$_3$I$_2$] for different sets of charges (— experiment, ⋯ Mulliken charges, - - - NPA charges and - ⋅ - neutral atoms). The simulated spectra were shifted in energy to match the experimental spectra: −0.5 eV for calculation with Mulliken charges, −2.5 eV with NPA charges and −9 eV with neutral atoms. (b) Experimental and calculated oxygen K-edge spectra of [UO$_2$(py)$_3$I$_2$] with Mulliken charges. Upper: comparison with polarized calculations by FDMNES with Mulliken charges (- - - polarized simulation ∥ O═U═O and ⋯ polarized simulation ⊥ O═U═O). Lower: comparison with the uranium density of states calculated by FDMNES with Mulliken charges (⋯ uranium 5f DOS and — uranium 6d DOS).

by −0.5 eV to match the experimental one, *versus* −2.5 eV for NPA charges and −9 eV for neutral atoms.

For all the calculations, the high-energy part of the experimental spectrum, encompassing an area from ∼ 545 to 570 eV is not well reproduced. It originates from the back-scattering process between the absorber and its nearest neighbour shells. This effect is due to the small radius of the cluster used for the calculation as confirmed by multiple scattering XANES calculations with a long cluster radius (not shown).

At this stage, we consider the experimental data to be accurately reproduced by the calculations with Mulliken charges. The good agreement between experiments and simulations obtained from Mulliken charges may be considered surprising since Mulliken charges are considered as poor descriptors of the electronic structure because of their strong dependency towards calculation details such as the size of the atom basis set. On the other hand NPA charges are altered much less by calculation details and are more reliable. Still, our results don't validate the use of Mulliken charges for describing uranyl compounds. They only mean that by using a Mulliken analysis and a particular combination of calculation parameters we can obtain a set of electronic charges from which we are able to significantly improve the simulation of the spectra. Further studies should be carried out to characterize more precisely the sensitivity of the calculation towards electronic charges.

To interpret the data, it is necessary to understand the transitions at the origin of NEXAFS features. During the process of the photoabsorption at the oxygen K-edge, a 1s electron is promoted to the oxygen empty 2p levels in the framework of the electric dipolar approximation. The oxygen K-edge XAS spectrum therefore reflects the empty or partially empty molecular orbitals having oxygen 2p character. Consequently, the K-shell XAS spectrum matches the LDOS of oxygen 2p orbitals. In the present case, the oxygen atoms are bound to uranium and comparison with the corresponding final state LDOS of uranium (which are calculated simultaneously by FDMNES) allows deduction of the hybridization of the vacant molecular orbitals with oxygen 2p character. The uranium 6d and 5f density of states are shown in Fig. 4b, together with the experimental and simulated spectra. Structures A and B can be attributed to the O 2p states hybridized with the U 5f ones, with possible participation of the 6d states in shoulder B. The highest energy peak C is due to hybridization between the oxygen 2p and the uranium 6d states. Their intensity is a fingerprint of the hybridization strength.

In order to describe more precisely the final antibonding molecular orbitals, polarization may be used, since the K-shell NEXAFS resonance intensities depend on the direction of the electric field vector $\vec{E}$ with respect to orbital orientation. Indeed, the resonance intensity associated with a specific molecular orbital final state is larger if the electric field vector is oriented along the direction of the maximum of the electron probability density of this molecular orbital, and the intensity vanishes if $\vec{E}$ is perpendicular to that direction, *i.e.*, if it lies in the nodal plane of the orbital.[28] Because **1** and **2** are poly-crystalline samples, polarized experiments are not possible. However, by performing polarized calculations parallel and perpendicular to the O═U═O unit, we are able to probe the

This journal is © the Owner Societies 2010

Phys. Chem. Chem. Phys., 2010, **12**, 14253–14262 | 14259

σ^* and the π^* antibonding molecular orbitals respectively. According to Fig. 4b, features A and C correspond to π^* antibonding molecular orbitals and shoulder B corresponds to a σ^* antibonding molecular orbital. Then, the order of the antibonding molecular orbitals is established as π_u^* (O 2p–U 5fπ) $<$ σ_u^* (O 2p–U 5fσ) $\sim$ σ_g^* (O 2p–U 6dσ) $<$ π_g^* (O 2p–U 6dπ). Denning found the same final state molecular orbital ordering for $[UO_2Cl_4]^{2-}$ but with differences in energies.[1] By comparing the energies of the final states, π_u^* and π_g^*, appear to be slightly more stabilized in the presence of pyridine than in the presence of chlorine. On the contrary, σ_u^* is more stabilized in the presence of chlorine than in the presence of pyridine.

The same procedure has been applied to the uranyl cyanido compound: $[UO_2(CN)_5][NEt_4]_3$. The calculated oxygen K-edge spectra with neutral atoms and Mulliken charges (Table 4) are shown in Fig. 5a, together with the experimental spectrum. As in the case of compound **1**, the spectrum calculated with Mulliken charges agrees well with the experimental data, whereas calculation with neutral atoms is not satisfactory. The agreement with the experimental spectra is quite good and the positions and relative heights of the three principal peaks are well reproduced by the calculation. As for compound **1**, the simulation of the Fermi level is improved with the Mulliken charges compared to neutral atoms. The uranium density of states and polarized calculations allow us to assign the experimental features (Fig. 5b). The order of the molecular orbitals is the same as for uranyl pyridine: π_u^* (O 2p–U 5fπ) $<$ σ_u^* (O 2p–U 5fσ) $\lesssim$ π_g^* (O 2p–U 6dπ), but with differences in energies and relative intensities. According to the LDOS calculations, the antibonding molecular orbital σ_u^* is split in uranyl cyanide whereas it is not in the uranyl pyridine. Moreover, an additional orbital arises near the σ_u^* one, with π symmetry (Fig. 5b). These characteristics are explained by the strong interaction between the σ_u^* and π_g^* molecular orbitals of the uranyl and the π_{CN}^* orbital. This leads to a broadening of peak b in the experimental spectrum of $[UO_2(CN)_5][NEt_4]_3$. It was explained in 3.3 that the hybridization of the π_{CN}^* orbital with the π_g^* orbital of uranyl gives rise to a π_g^* molecular orbital at a lower energy than the σ_u^* orbital. One can see the appearance of a new peak and then the broadening of peak b in Fig. 5b, showing the polarized calculation. Furthermore, the molecular orbital diagram calculation indicates that the participation of the uranyl orbital is very small, explaining why there is almost no density of uranium states at this energy. In the uranyl cyanide compound, the strong π donation of the cyanide ligand also shifts peak c (π_g^* molecular orbitals of the uranyl) towards higher energies. With the aid of quantum chemical calculations of the electronic structure we were able to reproduce the oxygen K-edge spectra and assign their features to the corresponding antibonding molecular orbitals. This approach has allowed us to emphasize differences in the electronic structure of two U═O bonds having almost the same length.

4. Conclusion

We have studied the electronic structure of the two uranyl compounds $[UO_2(py)_3I_2]$ and $[UO_2(CN)_5][NEt_4]_3$ using NEXAFS spectroscopy, simulation and quantum chemistry
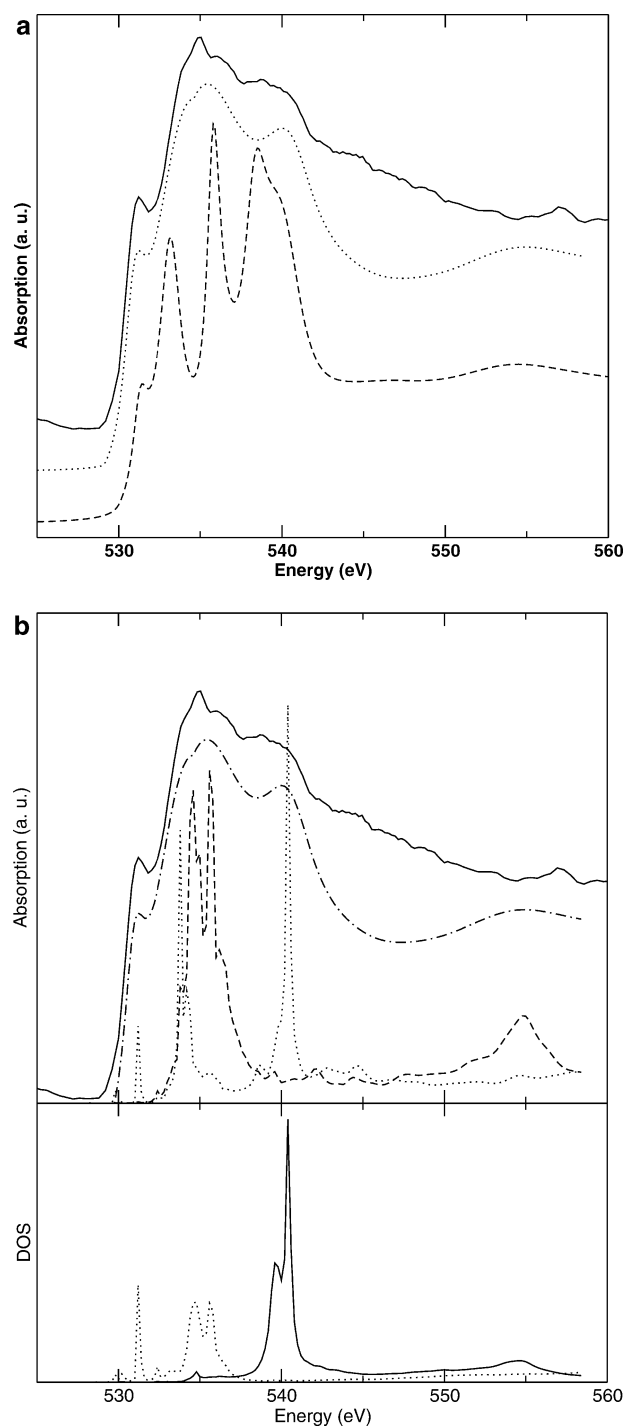
Fig. 5 (a) Experimental and calculated oxygen K-edge spectra of $[UO_2(CN)_5][NEt_4]_3$ for different sets of charges (—experiment, $\cdots$ Mulliken charges, - - - neutral atoms). The simulated spectra are shifted in energy to match the experimental spectra: -1.8 eV for calculation with Mulliken charges and -6.5 eV with neutral atoms. (b) Experimental and calculated oxygen K-edge spectra of $[UO_2(CN)_5][NEt_4]_3$ with Mulliken charges. Upper: comparison with polarized calculations by FDMNES with Mulliken charges (- - - polarized simulation $\parallel$ O═U═O and $\cdots$ polarized simulation $\perp$ O═U═O). Lower: comparison with the uranium density of states calculated by FDMNES with Mulliken charges ($\cdots$ uranium 5f DOS and — uranium 6d DOS).

calculations. To establish a relationship between the NEXAFS spectra and the electronic structure of the compounds, we have used ground-state DFT calculations and NEXAFS experiments together with simulations as complementary tools. The unique way of combining these theoretical methods with one experimental technique has allowed us to extract electronic structure information from the experimental spectra. In the first step we determined the ground-state electronic structure of the uranyl complexes and then simulated the NEXAFS spectra using a finite difference method as implemented in FDMNES and the TD-DFT approach. To improve the FDMNES simulation and to investigate the influence of the electronic structure on the NEXAFS, we have used the results obtained from the ground-state electronic structure calculations (with ADF) as inputs in the FDMNES simulations. The results show that simulated NEXAFS spectra are very sensitive to the electronic structure of the complexes and that we are able to accurately simulate the experimental spectra by using Mulliken electronic charges. While experimental spectra give a representation of the oxygen 2p orbitals, the calculations complete this picture with the uranium 5f and 6d orbitals. Hence the unoccupied molecular orbital diagram can be partially constructed. TD-DFT transition energies are roughly equal to the energy difference between the core orbital and the valence molecular orbital involved in the transition. The TD-DFT approach used here with a limited size atomic basis set does not perform as well as FDMNES especially at the higher energy region where energy shifts between electronic transitions tend to be underestimated by the calculation. However the TD-DFT calculations yield the transitions in terms of a molecular orbital picture. By comparing the TD-DFT with FDMNES results, we were able to relate electronic structure calculations and experimental spectra.

Despite their structural similarities, in particular very close uranium–oxygen bond distances, we have found significant differences in the electronic structure of $\{UO_2\}^{2+}$ entities, explained by differences in bonding between $\{UO_2\}^{2+}$ and the equatorial ligands. According to the molecular orbital diagrams of the two compounds, the cyanide π and σ occupied molecular orbitals interact with the uranyl π and σ orbitals whereas the pyridine interacts only through its σ orbitals. The ability of the cyanide ion to induce π-type interactions with uranyl is also apparent in the diagram of the unoccupied molecular orbitals. It results in the appearance of a new transition in the oxygen K-edge spectra of the cyanido compound when compared to the uranyl–pyridine complex. The cyanide π-type interaction takes place mostly with uranyl π_g^* or π_g involving 6d orbitals. According to the MO calculation, it is stronger with unoccupied orbitals than with occupied π_g molecular orbitals. This may explain why it has a strong effect on the NEXAFS spectrum while the uranium–oxygen bond distances are not strongly altered.

References

1 R. G. Denning, *J. Phys. Chem. A*, 2007, **111**, 4125–4143.
2 B. E. Bursten and R. J. Strittmatter, *Angew. Chem., Int. Ed. Engl.*, 1991, **30**, 1069–1085.
3 J. Li and B. E. Bursten, *J. Am. Chem. Soc.*, 1997, **119**, 9021–9032.
4 M. Pepper and B. E. Bursten, *Chem. Rev.*, 1991, **91**, 719–741.
5 Z. M. Sabirov and A. A. Bagatur'yants, *Russ. Chem. Rev.*, 1991, **60**, 1059.
6 G. Cavigliasso and N. Kaltsoyannis, *Inorg. Chem.*, 2007, **46**, 3557–3565.
7 B. O. Roos, P. Malmqvist and L. Gagliardi, *J. Am. Chem. Soc.*, 2006, **128**, 17000–17006.
8 J. Wiebke, A. Moritz, X. Cao and M. Dolg, *Phys. Chem. Chem. Phys.*, 2007, **9**, 459–465.
9 A. C. Tsipis, C. E. Kefalidis and C. A. Tsipis, *J. Am. Chem. Soc.*, 2008, **130**, 9144–9155.
10 K. T. Moore and G. van der Laan, *Rev. Mod. Phys.*, 2009, **81**, 235.
11 D. Páez-Hernández, R. Ramírez-Tagle, E. Codorniu-Hernández, L. A. Montero-Cabrera and R. Arratia-Pérez, *Polyhedron*, 2010, **29**, 975–984.
12 S. Fortier and T. W. Hayton, *Coord. Chem. Rev.*, 2010, **254**, 197–214.
13 J. Berthet, G. Siffredi, P. Thuery and M. Ephritikhine, *Dalton Trans.*, 2009, 3478–3494.
14 G. Nocton, P. Horeglad, J. Pecaut and M. Mazzanti, *J. Am. Chem. Soc.*, 2008, **130**, 16633–16645.
15 T. W. Hayton and G. Wu, *Inorg. Chem.*, 2009, **48**, 3065–3072.
16 J. Berthet, P. Thuery, J. Dognon, D. Guillaneux and M. Ephritikhine, *Inorg. Chem.*, 2008, **47**, 6850–6862.
17 J. Maynadié, J. Berthet, P. Thuery and M. Ephritikhine, *Chem. Commun.*, 2007, 486–488.
18 I. Charushnikova and C. Den Auwer, *Koord. Khim.*, 2007, **33**, 53–60.
19 J. Berthet, M. Nierlich and M. Ephritikhine, *Dalton Trans.*, 2004, 2814–2821.
20 M. J. Sarsfield, M. Helliwell and J. Raftery, *Inorg. Chem.*, 2004, **43**, 3170–3179.
21 B. Masci, M. Nierlich and P. Thuery, *New J. Chem.*, 2002, **26**, 120–128.
22 A. Vaughn, C. Barnes and P. Duval, *Angew. Chem., Int. Ed.*, 2007, **46**, 6622–6625.
23 C. Villiers, P. Thuéry and M. Ephritikhine, *Angew. Chem., Int. Ed.*, 2008, **47**, 5892–5893.
24 M. Ephritikhine, *Dalton Trans.*, 2006, 2501–2516.
25 G. S. Groenewold, A. K. Gianotto, M. E. McIlwain, M. J. Van Stipdonk, M. Kullman, D. T. Moore, N. Polfer, J. Oomens, I. Infante, L. Visscher, B. Siboulet and W. A. de Jong, *J. Phys. Chem. A*, 2008, **112**, 508–521.
26 D. L. Clark, S. D. Conradson, R. J. Donohoe, D. W. Keogh, D. E. Morris, P. D. Palmer, R. D. Rogers and C. D. Tait, *Inorg. Chem.*, 1999, **38**, 1456–1466.
27 Y. Joly, *J. Synchrotron Radiat.*, 2002, **10**, 58–63.
28 J. Stöhr, *NEXAFS spectroscopy*, Springer, 1996.
29 F. Jollet, T. Petit, S. Gota, N. Thromat, M. Gautier-Soyer and A. Pasturel, *J. Phys.: Condens. Matter*, 1997, **9**, 9393.
30 H. Modrow, S. Bucher, J. J. Rehr and A. L. Ankudinov, *Phys. Rev. B: Condens. Matter Mater. Phys.*, 2003, **67**, 035123.
31 Y. Joly, *Phys. Rev. B: Condens. Matter Mater. Phys.*, 2001, **63**, 125120.
32 ADF2008, SCM, Theoretical Chemistry, Vrije Universiteit, Amsterdam, The Netherlands, http://www.scm.com, 2008.
33 C. Fillaux, J. Berthet, S. D. Conradson, P. Guilbaud, D. Guillaumont, C. Hennig, P. Moisy, J. Roques, E. Simoni, D. K. Shuh, T. Tyliszczak, I. Castro-Rodriguez and C. Den Auwer, *C. R. Chimie*, 2007, **10**, 859–871.
34 C. Fillaux, C. Den Auwer, D. Guillaumont, D. K. Shuh and T. Tyliszczak, *J. Alloys Compd.*, 2007, **444–445**, 443–446.

This journal is © the Owner Societies 2010

Phys. Chem. Chem. Phys., 2010, **12**, 14253–14262 | 14261

35 J. Berthet, M. Nierlich and M. Ephritikhine, *Chem. Commun.*, 2004, 870–871.

36 J. Berthet, P. Thuery and M. Ephritikhine, *Chem. Commun.*, 2007, 604–606.

37 H. Nilsson, T. Tyliszczak, R. Wilson, L. Werme and D. Shuh, *Anal. Bioanal. Chem.*, 2005, **383**, 41–47.

38 E. van Lenthe, A. Ehlers and E. J. Baerends, *J. Chem. Phys.*, 1999, **110**, 8943–8953.

39 A. D. Becke, *Phys. Rev. A: At., Mol., Opt. Phys.*, 1988, **38**, 3098.

40 J. P. Perdew, *Phys. Rev. B: Condens. Matter*, 1986, **33**, 8822.

41 E. D. Glendening and J. K. Badenhoop, *NBO 5.0*, 2001.

42 M. Stener, G. Fronzoni and M. de Simone, *Chem. Phys. Lett.*, 2003, **373**, 115–123.

43 S. J. A. van Gisbergen, J. G. Snijders and E. J. Baerends, *Comput. Phys. Commun.*, 1999, **118**, 119–138.

44 M. Krause and J. Oliver, *J. Phys. Chem. Ref. Data*, 1979, **8**, 329–338.

45 J. L. Sonnenberg, P. J. Hay, R. L. Martin and B. E. Bursten, *Inorg. Chem.*, 2005, **44**, 2255–2262.

46 J. C. Slater and K. H. Johnson, *Phys. Rev. B: Solid State*, 1972, **5**, 844.

47 M. Stener, A. Lisini and P. Decleva, *Chem. Phys.*, 1995, **191**, 141–154.

48 M. E. Casida, *THEOCHEM*, 2009, **914**, 3–18.

49 S. DeBeer George, T. Petrenko and F. Neese, *J. Phys. Chem. A*, 2008, **112**, 12936–12943.

50 K. Ray, S. D. George, E. I. Solomon, K. Wieghardt and F. Neese, *Chem.–Eur. J.*, 2007, **13**, 2783–2797.

51 S. A. Kozimor, P. Yang, E. R. Batista, K. S. Boland, C. J. Burns, D. L. Clark, S. D. Conradson, R. L. Martin, M. P. Wilkerson and L. E. Wolfsberg, *J. Am. Chem. Soc.*, 2009, **131**, 12125–12136.

52 O. V. Gritsenko, P. R. T. Schipper and E. J. Baerends, *Chem. Phys. Lett.*, 1999, **302**, 199–207.

14262 | *Phys. Chem. Chem. Phys.*, 2010, **12**, 14253–14262

This journal is © the Owner Societies 2010